metals

MDPI

Article

Texture Evolution in Biocompatible Mg-Y-Re Alloy After Friction Stir Processing

Lenka Kunčická [1,*], Petr Král [1], Jiří Dvořák [1] and Radim Kocich [2]

[1] Institute of Physics of Materials, ASCR, 61662 Brno, Czech Republic; pkral@ipm.cz (P.K.); dvorak@ipm.cz (J.D.)
[2] VŠB—Technical University of Ostrava, 17. listopadu 15, 708 00 Ostrava 8, Czech Republic; radim.kocich@vsb.cz
* Correspondence: kuncicka@ipm.cz; Tel.: +420-532-290-371

Received: 30 September 2019; Accepted: 29 October 2019; Published: 1 November 2019

Abstract: The presented study deals with the investigation of biocompatible WE 43 Mg-based alloy processed via the combination of rotary swaging (RS) and friction stir processing (FSP) at three different rotational speeds of 400 RPM, 800 RPM, and 1200 RPM. The structure observations primarily focused on texture development and characterizations of grain sizes and grain boundaries. The results showed that swaging plus processing at 400 RPM and 1200 RPM lead to substantial recrystallization and grain refinement. The fractions of low angle grain boundaries within the 400 RPM and 1200 RPM samples were approximately 11%, while for the 800 RPM sample exhibiting secondary recrystallization it was about 22%. The grains were also the finest in the 1200 RPM sample (average grain diameter of 1.8 μm). The processed structures exhibited a slight tendency to form the {10-10} <0001> preferential fiber texture (especially the 800 RPM sample). Tensile testing showed the FSP to have positive influence on the ultimate tensile stress, as well as ductility of all the samples; the mechanical properties improved with increasing FSP rate.

Keywords: magnesium alloys; grains and interfaces; microstructure; texture

---

1. Introduction

Their advantageous properties, such as low density, good castability and machinability, favourable specific strength, and superior thermal and electrical conductivity, make magnesium-based alloys perspective solutions for demanding applications, such as lightweight structures, transportation equipment, and aircraft or jet engines [1,2]. Given by their favourable biocompatibility, light weight, and low elastic modulus similar to the moduli of human bones, selected Mg-based alloys are also applicable for biodegradable implant components [3–5]. The mechanical and physical properties of pure Mg are not exceptional, however, they can be enhanced—primarily in the two following ways.

The first way is addition of alloying elements. The Mg-Al and Mg–Zn systems are popular for constructional purposes [6], additions of zinc are advantageous also for biocompatible Mg alloys [3]. Optimized additions of rare earth (RE) elements have superior effects on enhancement of properties of Mg; Mg-Zn-Y based alloys were reported to feature good cytocompatibility and to have positive antibacterial effects [7,8]. RE, such as Y, Nd, Dy, or Gd generally improve the corrosion resistance of Mg-based alloys and support grain refinement and improvement and homogenization of the mechanical properties [9–12]. RE elements have also been shown to reduce the critical resolved shear stress (CRSS) for non-basal slip systems and tetragonal aspect ratio of prismatic and pyramidal slip systems, which consequently increases formability (generally low for pure Mg) [13]. The beneficial effects of Yttrium are numerous, it increases formability, supports texture randomization and activation of non-basal slip systems by lowering the matrix energy and promoting solute drag (similarly to neodymium [14]), which further decreases anisotropy of the mechanical properties [15].

The second way of enhancement of Mg-based alloys' properties is via structure changes imparted by innovative plastic deformation technologies, which have drawn attention not only for their ability to effectively refine structural units and consequently enhance the final properties of the processed materials, but also for their ability to process materials with relatively low formabilities [16–18]. The most effective technologies are the methods of severe plastic deformation (SPD), such as equal channel angular pressing (ECAP) [19,20], accumulative roll bonding (ARB) [21], high pressure torsion (HPT) [22], or rotary swaging (RS) [23,24] and friction stir processing and welding—FSP and FSW [25]. Previously published studies investigated the effects of the most efficient SPD methods—ECAP (e.g., Kocich et al. [26] reported the effects of friction and die angle parameters on deformation behaviour of the AZ63 alloy, and Cabibbo et al. [27] reported the grain size within the WN43 to decrease down to 380 nm after 8 ECAP passes), and HPT (proven to be effective for homogenization of distribution of RE-based precipitates [28]) on various Mg-based alloys. However, the main drawback of these methods is that they are limited to relatively small samples of definite dimensions (the largest known HPT-processed samples have the diameters of approximately 20–30 mm). On the other hand, technologies such as RS and FSP can be designed to process large bulk samples.

RS is an intensive plastic deformation process enabling reduction of diameters of axisymmetric products by a repeated action of rotating dies affecting opposite surfaces of the swaged-piece with compressive swaging forces having two components, axial and tangential [29,30]. The axial component contributes primarily to elongation of the final product, whereas the tangential component introduces shear strain contributing to fragmentation of the grains and accumulation of dislocations leading to subsequent formation of dislocation cells and subgrains, and consequent grain refinement. FSP imposes severe shear strain to thin layers of materials, which generally introduces substantial grains' recrystallization. The method is advantageous especially for final processing of demanding materials [31,32]. Besides their versatility, both the RS and FSP methods contribute substantially to structure homogenization, progressive grain refinement, and enhancement of utility and mechanical properties.

Reports on the effects of swaging on Mg-based alloys are not numerous. Gan et al. [33,34] studied the effects of swaging on commercially pure cast Mg and found progressive grain refinement and the tendency of the swaged material to form the (0002) basal texture. Wang et al. [35] investigated the optimum swaging/annealing conditions for WE43 alloy and increased both, the strength and ductility of the alloy via swaging and annealing at 400 °C, and Martynenko et al. [36,37] optimized the swaging treatment and reported the grains within WE43 alloy to refine down to 0.5 µm and the strength to increase to more than 400 MPa after severe swaging at temperatures between 325 and 400 °C. Several studies reporting the effects of FSP on Mg-based alloys have been published, but they are scarce. Wang et al. [38] documented the positive effect of rotational speed of FSP on mechanical properties of the processed Mg–Zn–Y–Zr sample, Kumar et al. [39] reported the positive influence of FSP on grain refinement within a laser-produced WE43 sample and characterized the varying strengthening mechanisms, Vargas et al. [40] imparted significant grain refinement (grain size of 1.2 µm after single FSP pass and submicron grain size after the second pass) and ductility increase within Mg-Zn-Ca-Zr samples, Liu et al. [41] homogenized the grain size and refined the grains down to approx. 2 µm and improved the corrosion resistance of Mg–9Li–1Zn alloy via texture randomisation, and Khan et al. [42] increased the ductility of QE22 alloy to almost 25% via imparting nucleation of new grains and texture alteration.

In order to study mutual effects of the two above characterized advantageous SPD technologies, the presented study deals with the investigation of a cast and solution treated Mg–based Mg-4Y-3Nd (WE43) alloy processed via rotary swaging (RS) and subsequent friction stir processing (FSP) under three different rotational speeds. The structures were studied via scanning electron microscopy;

the analyses focused primarily on characterization of grains and their boundaries and on texture characterization. The mechanical properties were examined via tensile tests.

2. Materials and Methods

The Mg-4Y-3Nd (WE43) alloy was produced by vacuum induction melting (VIM), cast, and further processed via rotary swaging (RS). Within this study, RS was implemented primarily to increase formability and homogenize the cast WE43 alloy structure. The final reduction ratio calculated using Equation (1), where S_0, S_n are the cross-section areas at the input and output of the swaging dies, respectively, was 1.20.

$$\varphi = \ln\left(\frac{S_0}{S_n}\right), \tag{1}$$

Swaging was followed by T4 heat treatment—8 hours' dwell at 520 °C, and final quenching in water (annealing procedure similar to our previous studies [12,28]). After the solution treatment (ST), samples of the dimensions of 40 × 20 × 20 mm were cut using electric discharging machine (Sodick SL400Q, Sodick Europe, Ltd, Warwick, UK) and mechanically polished. The prepared samples were further subjected to FSP processing at the traverse rate of 60 mm·min^{-1} and three different rotational speeds of 400 RPM, 800 RPM, and 1200 RPM, and subsequently quenched in water. The conical friction tool with a 3 mm long pin with the diameter varying from 6 mm to 4 mm was made of a tool steel and had a flat shoulder with 15 mm in diameter (similar set up as e.g., in refs. [31,39]). The schematics of the entire production process in depicted in Figure 1.

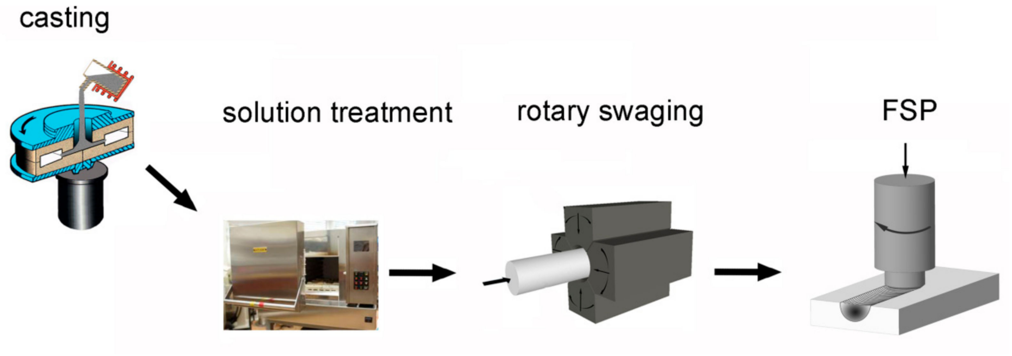

Figure 1. Schematic depiction of production process. FSP: friction stir processing.

After processing, samples for structure analyses taken in the direction of friction tool movement were mechanically ground and polished, and finally polished electrolytically. The structures of the FSP-processed, as well as of the rotary swaged and solution treated (RS-ST) material states were scanned via Tescan Lyra 3 scanning electron microscope (TESCAN Brno s.r.o, Brno, Czech Republic) equipped with an electron backscatter diffraction (EBSD) detector (Oxford Instruments, Abingdon-on-Thames, UK). The scans taken with the steps of 0.25 µm were evaluated using OXFORD Instruments [43] software (Oxford Instruments, Abingdon-on-Thames, UK). The grain size was determined as the arithmetic average of the results of measurements taken in two perpendicular (horizontal, vertical) directions. The misorientation angle θ = 15° was set as the minimum angle for identification of grains with high angle grain boundaries (HAGBs), the boundaries with θ lower than 15° are denoted as low angle grain boundaries (LAGBs). The grain is characterized as a recrystallized grain when the internal average misorientation angle in the grain is lower than 1°. In the case the grain contains subgrain boundaries with misorientation angles higher than 1°, the grain is characterized as substructured. The values of the internal average misorientation angles higher than 1° are characteristic for deformed grains. The textures were evaluated in the direction perpendicular to the direction of friction pin movement and were evaluated by using 20° maximal deviation from the specific texture components.

The specimens for tensile testing were cut via electro-discharging machine in the direction parallel to the direction of friction tool movement. The tensile tests specimens were 10 mm long and had

2 × 4 mm cross-sections, the room temperature tests were carried out with the strain rate of 10^{-3} s^{-1} using a Zwick testing machine (Zwick/Roell—Messphysik KAPPA LA, Zwick / Roell CZ s.r.o., Brno, Czech Republic). The final ultimate tensile strength and elongation were calculated as the average value from three individual tested samples.

3. Results

3.1. Grains and Boundaries Characterization

The results of grain size analyses for the rotary swaged and solution-treated (RS-ST) material and the samples after RS and FSP are shown in Figure 2a–d. The mean grain size for the RS-ST sample was 58.5 µm. The grains refined to the average diameters of 4.2 µm, 7.1 µm, and 1.8 µm, after RS plus 400, 800, and 1200 RPM FSP, respectively. These results indicate that all the FSP technologies led to significant grain refinement within the WE43 alloy. The FSP rate of 1200 RPM even led to the formation of structure the average grain size within which approached the ultra-fine (UF) level, and approximately 18% of the grains within this sample were smaller than 1 µm. The grains were the coarsest in the 800 RMP sample.

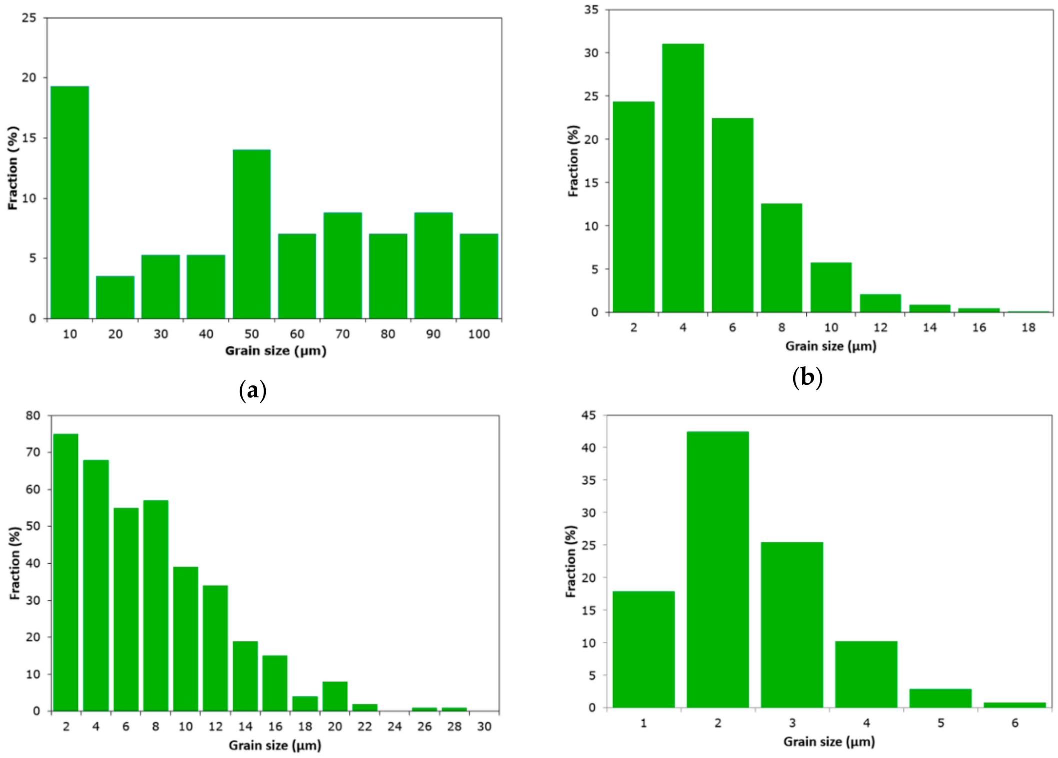

(**a**) (**b**)

(c) (d)

Figure 2. Grain size distributions for samples: Rotary swaged and solution treated (RS-ST) (**a**); RS+400 RPM FSP (**b**); RS+800 RPM FSP (**c**); RS+1200 RPM FSP (**d**).

The analyses of grain boundaries showed that the RS-ST sample featured a vast majority of high angle grain boundaries (HAGBs); Figure 3a shows the cast structure of the prepared WE43 alloy, whereas Figure 3b depicts the RS-ST band contrast EBSD image with HAGBs highlighted in green, and Figure 3c shows the corresponding misorientations chart for the RS-ST sample.. The image also clearly documents the presence of relatively coarse precipitates. After RS+400 RPM FSP, the fraction of low angle grain boundaries (LAGBs) increased to approximately 11%; Figure 3d depicts the EBSD image with HAGBs in green, while Figure 3e shows corresponding misorientations chart. This phenomenon indicates the development of substructure due to the severe imposed strain imparting accumulation of structure defects (dislocations), which further cluster into tangles, cells, and dislocations walls and eventually form LAGBs [44]. Figure 3f,g depict the EBSD image with highlighted HAGBs and misorientations chart, respectively, for the RS+800 RPM FSP sample. The fraction of LAGBs for this sample increased to 16%. RS+1200 RMP FSP processing introduced LAGBs fraction similar to RS+400 RPM processing, i.e., approximately 11% (Figure 3h,i).

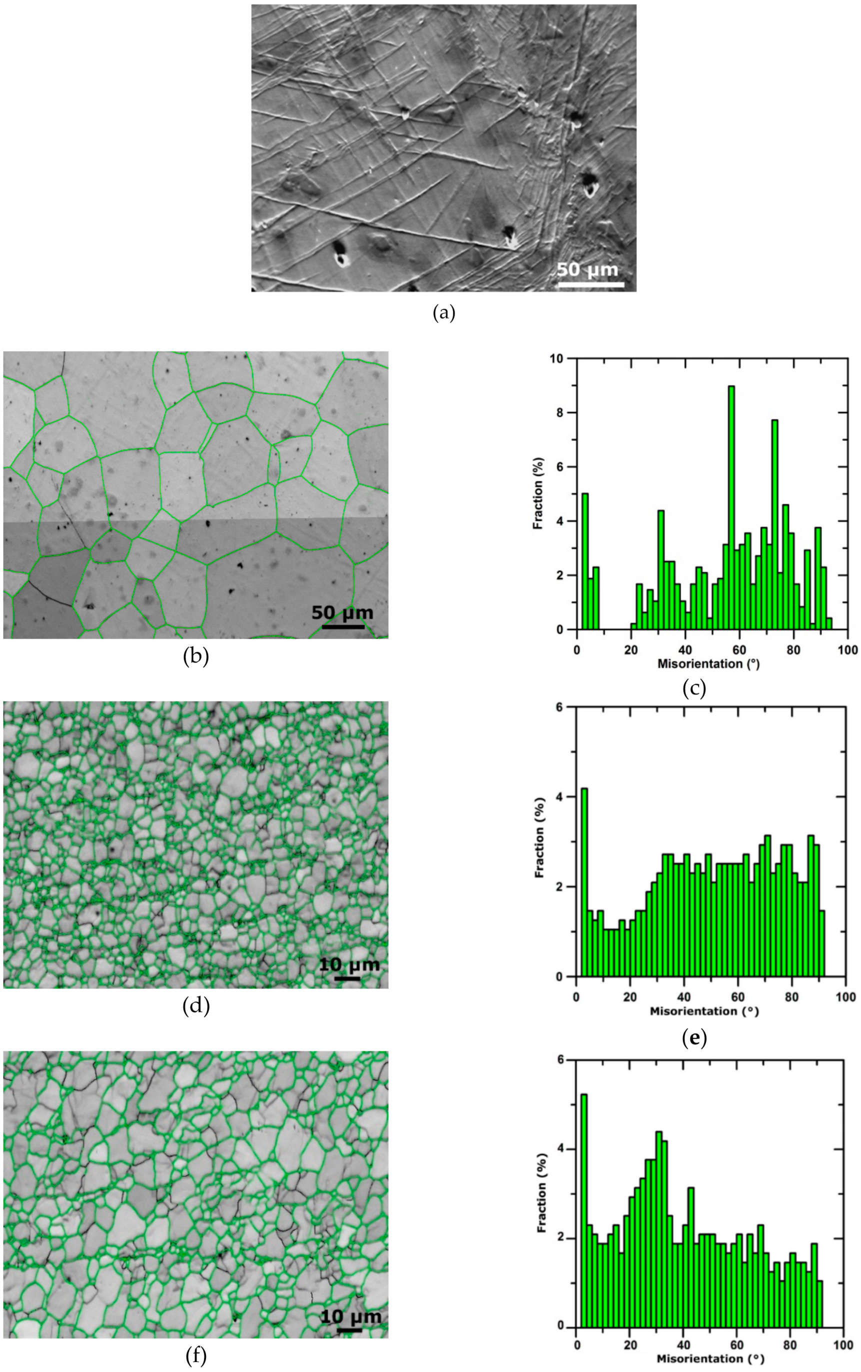

(a)

(b)

(c)

(d)

(**e**)

(f)

(g)

Figure 3. *Cont.*

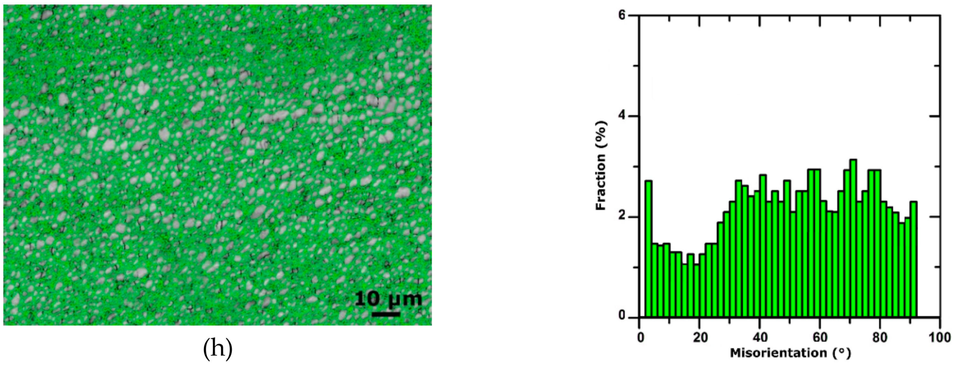

(h) (i)

Figure 3. SEM-BSE scan of cast structure (**a**); band contrast electron backscatter diffraction (EBSD) image with high angle grain boundaries (HAGBs) highlighted in green for samples: RS-ST (**b**); RS+400 RPM FSP (**d**); RS+800 RPM FSP (**f**); RS+1200 RPM FSP (**h**). Grain boundaries misorientations distributions for samples: RS-ST (**c**); RS+400 RPM FSP (**e**); RS+800 RPM FSP (**g**); RS+1200 RPM FSP (**i**).

3.2. Recrystallized Fraction

The above-mentioned analyses can be confirmed via examinations of recrystallized fraction. Figure 4a demonstrates an example of evaluation of the analyses of the recrystallized (green colour), substructured (yellow colour), and deformed (red colour) fractions for the RS+400 RPM FSP sample. Figure 4b then summarizes the results of the analyses for all the processed samples. Obviously, the fraction of growing grains with developed substructure was the highest for the RS+800 RPM FSP sample. The RS+1200 RPM FSP sample, the imposed energy for which was increased to the level sufficient for further grains restoration (also supported by the highest actual processing temperature), featured the highest fraction of recrystallized grains. This result is in accordance with the grains size analyses, as well as texture analyses reported in Section 3.3.

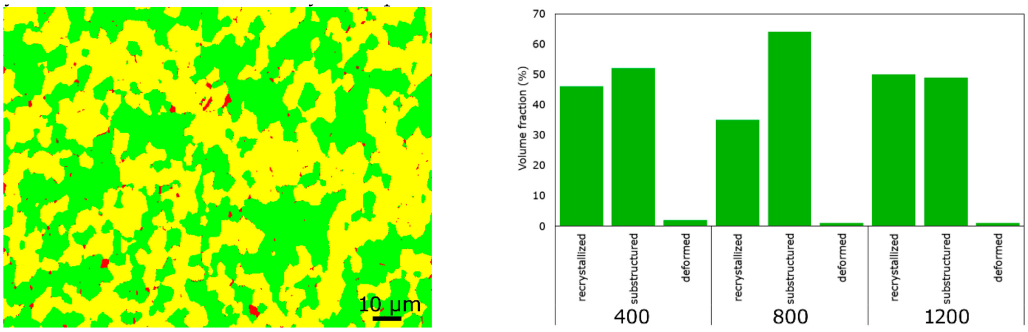

(a) (b)

Figure 4. Recrystallized, substructured, and deformed fractions: example of analyses evaluation for RS+400 RMP FSP sample (**a**); summary for RS+FSP-processed samples (**b**).

3.3. Texture

The textures for all the RS-ST, and RS plus 400 RPM, 800 RPM, and 1200 RPM FSP samples were evaluated with the emphasis on the possible presence of preferential fibers/orientations and their intensities, and on the correlation of preferential orientations and recrystallized fractions. Figure 5a–d depict inverse pole figures (IPFs) for the RS-ST, and RS plus 400 RPM, 800 RPM, and 1200 RPM FSP samples, respectively, with highlighted prevailing ideal orientations -{0001} <11-20> in green colour, and {0001} <10-10> in red colour. Figure 6a–d then depict IPFs with texture intensities for the mentioned samples. Last but not least, Figure 7a–d show pole figures (PF) depicting recrystallized grains for the RS-ST, and RS plus 400 RPM, 800 RPM, and 1200 RPM FSP samples, respectively. In the

PFs, the colours characterize the individual grain sizes from blue for the new smallest recrystallized grains, through green for the growing grains, to red for the largest ones.

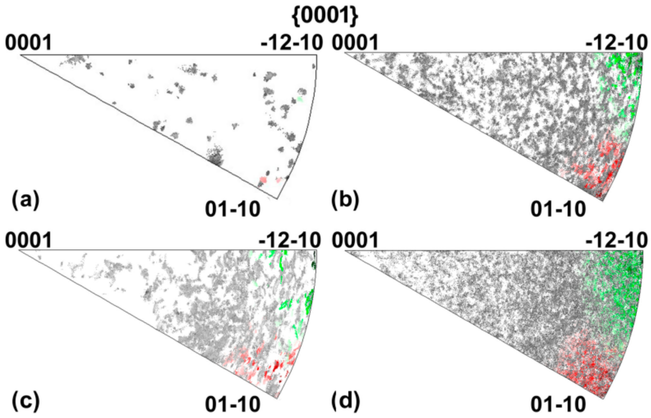

Figure 5. Inverse Pole Figures for samples: RS-ST (**a**); RS+400 RPM FSP (**b**); RS+800 RPM FSP (**c**); RS+1200 RPM FSP (**d**). Orientation {0001} <10-10> depicted in red, orientation {0001} <11-20> depicted in green.

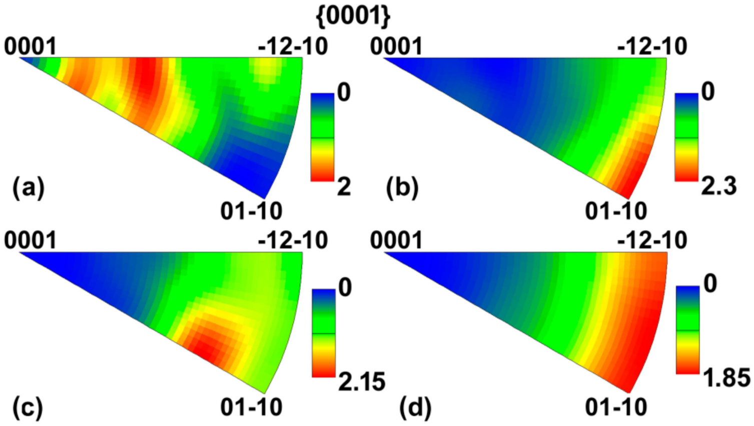

Figure 6. Inverse pole figures for samples: RS-ST (**a**); RS+400 RPM FSP (**b**); RS+800 RPM FSP (**c**); RS+1200 RPM FSP (**d**).

The RS-ST sample obviously featured randomly scattered grains with no preferential orientations (Figures 5a and 7a), the IPF depicted in Figure 6a shows that the maximum texture intensity for this sample was less than 2 times random and the grains did not clearly incline to a single distinguishable orientation. After RS+400 RPM FSP processing, the grains refined significantly and the fresh newly nucleated grains (blue dots in Figure 7b) did not exhibit any preferential texture orientation. Nevertheless, the growing grains exhibited the tendency to form the {0001} <11-20> and {0001} <10-10> preferential textures (Figures 5b and 6b). The latter was more intense, as depicted in Figure 6b, although its total intensity was only slightly higher than 2 times random. Mutual correlation of Figures 6b and 7b imparts the supposition that the growing grains had the tendency to align along the {0001} <11-20> preferential orientations at first, and later on, as they continued to grow, tended to acquire the {0001} <10-10> orientation. This conclusion about texture evolution is supported by Figure 5c, Figure 6c, and Figure 7c depicting the IPFs and PFs for the RS+800 RPM FSP sample, which exhibited similar tendencies; the maximum intensities of the preferential texture orientations were again approximately two times random for this sample. Nevertheless, the <10-10> ideal texture orientation was approximately by 25° shifted, which is evident in Figures 6c and 7c. The IPFs and PFs depicting texture characteristics for the RS+1200 RPM FSP processed sample can be seen in Figures

5d, 6d and 7d. The material exhibited fine grains having both the {0001} <11-20> and {0001} <10-10> preferential orientations in similar intensities.

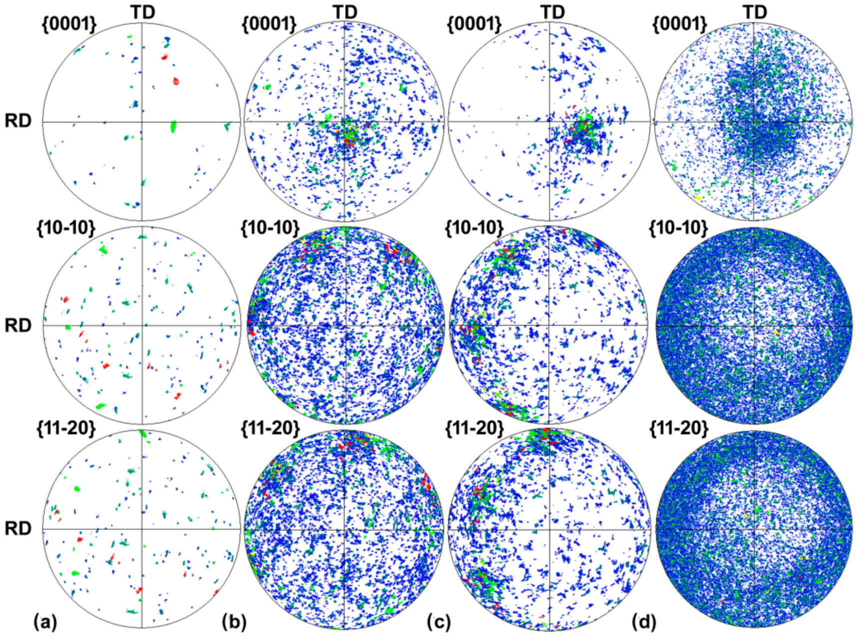

Figure 7. Pole figures emphasizing grains orientations in relation with grain growth for samples: RS-ST (**a**); RS+400 RPM FSP (**b**); RS+800 RPM FSP (**c**); RS+1200 RPM FSP (**d**).

3.4. Mechanical Testing

The samples taken from the cast material, material after RS and ST, and the materials after RS plus 400 RPM, 800 RPM, and 1200 RPM FSP were subjected to tensile tests, the results of which are summarized in Table 1. Evidently, plasticity of all the processed samples increased significantly when compared to the cast material. Rotary swaging in combination with solution treatment increased the ultimate tensile strength (UTS) to more than 200 MPa, and also increased the maximum elongation to failure. The RS+400 RPM and RS+800 RPM samples also featured both enhanced strength and elongation, however, the elongation of the RS+800 RPM sample was the lowest of all the deformation processed ones. RS+FSP at 1200 RPM led to the UTS increase up to almost 280 MPa.

Table 1. Mechanical properties for investigated material states.

Sample	YS (MPa)	UTS (MPa)	Elongation to Failure (%)
As cast	115	142 ± 15	3.8 ± 0.5
RS-ST	135	201 ± 10	5.8 ± 0.8
400 RPM	166	232 ± 22	10.9 ± 0.9
800 RPM	172	246 ± 19	9.2 ± 1.5
1200 RPM	184	279 ± 28	11.7 ± 1

4. Discussion

RS is known for its positive influence on grain refinement and fragmentation of larger particles and precipitates consequently resulting in enhanced properties of the processed materials [45,46]. Its favourable effects on improvement of mechanical properties were documented by others. For example, Wang et al. [35] previously reported the UTS for the WE43 alloy to increase to more than 350 MPa after swaging at 300 °C and subsequent annealing, however, their sample was subjected to the significant reduction ratio of 73% and featured the grain size of 4 µm after swaging. As proven by the herein presented results, the UTS of the RS-ST sample exceeded 200 MPa, but the elongation of this sample was substantially lower than of the samples after RS plus FSP processing. As obvious from Figure 3b, the RS-ST sample featured not only relatively large grains but also precipitated particles, which most probably nucleated in the material during cooling. The precipitates acted as obstacles for dislocations movement during the tensile deformation under cold conditions and resulted in higher UTS (compared to the cast material), but lower plasticity (compared to the FSP samples) [47].

Subsequent FSP imparted dissolution of most of the precipitates into solid solution, which slightly increased the UTS via solid solution strengthening, but primarily enhanced plasticity [48]. The analyses indicate that RS+FSP at 400 RPM introduced sufficient energy to impart formation of new grains within the structure. RS and processing at the FSP rate of 800 RPM imparted recrystallization, too. However, the increased imposed energy together with the higher actual processing temperature also caused grain coarsening and further substructure development—the fraction of growing grains with developed substructure was the highest for this sample—which slightly decreased the elongation to failure when compared to the other samples after FSP (the accumulated energy not only caused the post-process grain growth, but most probably also imparted re-nucleation of fine precipitates, however, these were not observed at the actual SEM magnification).

Chang et al. [49] previously documented the tendency of grains within extruded Mg-based AZ31 alloy subjected to FSP to coarsen with increasing FSP rate. This report is similar to the herein observed results of 400 RPM and 800 RPM samples. Primary recrystallization requires a certain amount of energy to be imposed into the processed material, but the energy necessary for the post-recrystallization grain growth is far smaller (by up to two orders of magnitude) [44]. By this reason, the accumulated energy in the 800 RPM sample, which was not consumed by the primary recrystallization, caused the grain boundaries to migrate to the point of energy exhaustion, which resulted in the increase in LAGBs fraction and introduced grain growth. However, the grain growth was inhomogeneous and occurred primarily in locations in which the new grains nucleated as first (shear bands, etc.) [44], which was documented also by Figure 2c, the presence of grains with the size of a few microns in which can be observed together with the presence of grains larger than 10 μm. Grains rearrangement occurring after the primary recrystallization was also documented by the promoted tendency of the grains to align along the {0001} <10-10> preferential texture orientation. Nevertheless, the ideal orientation was approximately by 25° shifted, which is evident in Figures 6c and 7c. Similar phenomenon was observed by Yuan and Mishra [50], who processed AZ31 alloy via 600–900 RPM FSP and found the basal textures to be tilted by approximately 35°. The herein presented lower deviation of approx. 25% can be attributed to the additions of Y and Nd, which aggravated grain boundary migration via solute drag [14].

Increasing the FSP rate to 1200 RPM further increased the imposed energy to the level sufficient for further recrystallization, which was also supported by the highest actual processing temperature. For this sample, the UTS as well as plasticity increased remarkably. The greatest contribution to this behaviour can be attributed to the significant grain refinement and formation of UFG structure with grains having more or less random orientations [50]. The RS+1200 RPM FSP sample featured the highest fraction of new grains without secondary grain growth. The increased imposed energy introduced via the increase in the FSP rotational rate to 1200 RPM imparted generation of new dislocations and the tendency of the structure to form new dislocation tangles, cells, and walls, and subsequent formation of LAGBs [48]. After reaching the critical level of accumulated energy, grains characterized with HAGBs start to form within the structure and the LAGBs fraction decreases [45]. The phenomenon of significant grain refinement after processing at 1200 RPM can be explained by the mutual effects of occurring recrystallization and the presence of RE elements supporting grain boundary pinning and formation of ultra-fine grains [51,52]. Similar conclusions were also drawn by Vargas et al. [40] for FPS-processed ZKX50 alloy containing Zr, the average grain size of which after processing by 1000 RPM was ~ 1 μm.

The generally very low maximum intensities of the preferential texture orientations demonstrate the favourable influence of Nd and Y on texture randomization. Texture randomisation supported by additions of RE in Mg-based biocompatible alloys was reported to contribute to the homogenization of mechanical and corrosion properties and lowering of anisotropy as regards the tension and compression loads, which consequently positively influences the fatigue life of the final product [7]. Torroni et al. [53] previously reported the fact that grain refinement together with dissolution of precipitates into solid solution increased the in vivo corrosion resistance of WE43 alloy and promoted osteogenesis at the implant/bone interface. Considering the mechanical properties and the structures of the herein studied swaged and friction stir processed samples, RS+800 RMP FSP processing would be promising for applications at elevated temperatures, since the creep behaviour can be expected to be the most favourable for this structure due to the relatively large grains [45]. On the other hand, for applications at room temperature, or at slightly elevated temperatures such as within the human body, the fine-grained RS+1200 RPM FSP sample structure can be considered to be the most favourable candidate.

5. Conclusions

The WE 43 magnesium-based alloy was subjected to rotary swaging (RS) followed by solution treatment (ST), and finally treated via friction stir processing (FSP) at three different rotational speeds of 400 RPM, 800 RPM and 1200 RPM.

Although RS+ST introduced grain refinement and improvement of the mechanical properties, the RS-ST-FSP combinations resulted in formation of new fine grains and further enhanced the properties. Both the samples processed via RS plus 400 RPM and 1200 RPM FSP featured newly crystallized grains with no significant intensity of preferential texture orientations, enhanced UTS, and the maximum elongation of more than 10% (the 1200 RPM sample exhibited UFG structure with the average grain size of less than 2 μm and the UTS of almost 280 MPa), all of which imparts promising application of both materials at temperatures close to the room or human body ones. On the other hand, the RS+800 RPM FSP sample exhibited substructure development and a relatively high fraction of low angle grain boundaries (LAGBs) resulting in slight texture formation and decrease in plasticity.

Author Contributions: Conceptualization, L.K., P.K., R.K.; methodology, L.K., R.K.; investigation, L.K, P.K., J.D.; data curation, P.K., J.D.; writing—original draft preparation, L.K.; writing—review and editing, L.K., R.K.; supervision, R.K.; project administration, L.K., R.K.; funding acquisition, L.K.

Funding: This research was financially supported by the Ministry of Education, Youth and Sports of the Czech Republic under projects m-IPMinfra (CZ.02.1.01/0.0/0.0/16_013/0001823).

Acknowledgments: The experimental material was prepared using equipment available at the Technical University of Ostrava. The research was performed with the equipment and base of IPMinfra research infrastructure.

Conflicts of Interest: The authors declare no conflict of interest. The funders had no role in the design of the study; in the collection, analyses, or interpretation of data; in the writing of the manuscript, or in the decision to publish the results.

References

1. Russell, A.; Lee, K.L. *Structure-Property Relations in Nonferrous Metals*, 1st ed.; John Wiley & Sons, Inc.: Hoboken, NJ, USA, 2005.
2. Seetharaman, R.; Lavanya, B.; Niharika, N.; Thyagarajan, P. Development and Performance Validation of Engine Oil Pump for Passenger Cars Using Magnesium Alloy. *Mater. Today Proc.* **2017**, *4*, 6743–6749. [CrossRef]
3. Bommala, V.K.; Krishna, M.G.; Rao, C.T. Magnesium matrix composites for biomedical applications: A review. *J. Magnes. Alloy.* **2019**, *7*, 72–79. [CrossRef]
4. Witte, F. The history of biodegradable magnesium implants: A review. *Acta Biomater.* **2010**, *6*, 1680–1692. [CrossRef] [PubMed]
5. Gu, X.N.; Zheng, Y.F. A review on magnesium alloys as biodegradable materials. *Front. Mater. Sci. China* **2010**, *4*, 111–115. [CrossRef]

6. Lukac, P.; Kocich, R.; Greger, M.; Padalka, M.; Szaraz, Z. Microstructure of AZ31 and AZ61 Mg alloys prepared by rolling and ECAP. *Kov. Mater.* **2007**, *45*, 115–120.
7. Hänzi, A.C.; Gerber, I.; Schinhammer, M.; Löffler, J.F.; Uggowitzer, P.J. On the in vitro and in vivo degradation performance and biological response of new biodegradable Mg-Y-Zn alloys. *Acta Biomater.* **2010**, *6*, 1824–1833. [CrossRef]
8. Feng, Y.; Zhu, S.; Wang, L.; Chang, L.; Hou, Y.; Guan, S. Fabrication and characterization of biodegradable Mg–Zn-Y-Nd-Ag alloy: Microstructure, mechanical properties, corrosion behavior and antibacterial activities. *Bioact. Mater.* **2018**, *3*, 225–235. [CrossRef]
9. Yang, L.; Huang, Y.; Peng, Q.; Feyerabend, F.; Kainer, K.U.; Willumeit, R.; Hort, N. Mechanical and corrosion properties of binary Mg-Dy alloys for medical applications. *Mater. Sci. Eng. B* **2011**, *176*, 1827–1834. [CrossRef]
10. Yang, L.; Huang, Y.; Feyerabend, F.; Willumeit, R.; Mendis, C.; Kainer, K.U.; Hort, N. Microstructure, mechanical and corrosion properties of Mg-Dy-Gd-Zr alloys for medical applications. *Acta Biomater.* **2013**, *9*, 8499–8508. [CrossRef]
11. Li, N.; Guo, C.; Wu, Y.H.; Zheng, Y.F.; Ruan, L.Q. Comparative study on corrosion behaviour of pure Mg and WE43 alloy in static, stirring and flowing Hank's solution. *Corros. Eng. Sci. Technol.* **2012**, *47*, 346–351. [CrossRef]
12. Kunčická, L.; Kocich, R. Comprehensive characterisation of a newly developed Mg-Dy-Al-Zn-Zr alloy structure. *Metals* **2018**, *8*, 73. [CrossRef]
13. Imandoust, A.; Barrett, C.D.; Al-Samman, T.; Inal, K.A.; El Kadiri, H. A review on the effect of rare-earth elements on texture evolution during processing of magnesium alloys. *J. Mater. Sci.* **2017**, *52*, 1–29. [CrossRef]
14. Jung, I.-H.; Sanjari, M.; Kim, J.; Yue, S. Role of RE in the deformation and recrystallization of Mg alloy and a new alloy design concept for Mg–RE alloys. *Scr. Mater.* **2015**, *105*, 1–6. [CrossRef]
15. Sandlöbes, S.; Zaefferer, S.; Schestakow, I.; Yi, S.; Gonzalez-Martinez, R. On the role of non-basal deformation mechanisms for the ductility of Mg and Mg–Y alloys. *Acta Mater.* **2011**, *59*, 429–439. [CrossRef]
16. Kocich, R.; Kursa, M.; Szurman, I.; Dlouhý, A. The influence of imposed strain on the development of microstructure and transformation characteristics of Ni–Ti shape memory alloys. *J. Alloys Compd.* **2011**, *509*, 2716–2722. [CrossRef]
17. Kapoor, R. Severe Plastic Deformation of Materials. In *Materials Under Extreme Conditions*, 1st ed.; Tyagi, A.K., Banerjee, S., Eds.; Elsevier: Amsterdam, The Netherlands, 2017; pp. 717–754. [CrossRef]
18. Kunčická, L.; Kocich, R.; Drápala, J.; Andreyachshenko, V.A. FEM simulations and comparison of the ECAP and ECAP-PBP influence on Ti6Al4V alloy's deformation behaviour. In *Proceedings of the Metal 2013, 22nd International Conference on Metallurgy and Materials, Brno, Czech Republic, 15–17 May 2013*; Tanger Ltd.: Ostrava, Czech Republic, 2013; pp. 391–396.
19. Kocich, R.; Greger, M.; Macháčková, A. Finite element investigation of influence of selected factors on ECAP process. In *Proceedings of the Metal 2010, 19th International Conference on Metallurgy and Materials, Brno, Czech Republic, 18–20 May 2010*; Tanger Ltd.: Ostrava, Czech Republic, 2010; pp. 166–171.
20. Kocich, R.; Szurman, I.; Kursa, M.; Fiala, J. Investigation of influence of preparation and heat treatment on deformation behaviour of the alloy NiTi after ECAE. *Mater. Sci. Eng. A.* **2009**, *512*, 100–104. [CrossRef]
21. Kocich, R.; Macháčková, A.; Fojtík, F. Comparison of strain and stress conditions in conventional and ARB rolling processes. *Int. J. Mech. Sci.* **2012**, *64*, 54–61. [CrossRef]
22. Kunčická, L.; Lowe, T.C.; Davis, C.F.; Kocich, R.; Pohludka, M. Synthesis of an Al/Al2O3 composite by severe plastic deformation. *Mater. Sci. Eng. A* **2015**, *646*, 234–241. [CrossRef]
23. Kocich, R.; Kunčická, L.; Macháčková, A.; Šofer, M. Improvement of mechanical and electrical properties of rotary swaged Al-Cu clad composites. *Mater. Des.* **2017**, *123*, 137–146. [CrossRef]
24. Kunčická, L.; Kocich, R.; Hervoches, C.H.; Macháčková, A. Study of structure and residual stresses in cold rotary swaged tungsten heavy alloy. *Mater. Sci. Eng. A* **2017**, *704*, 25–31. [CrossRef]
25. Nikulin, I.; Malopheyev, S.; Kipelova, A.; Kaibyshev, R. Effect of SPD and friction stir welding on microstructure and mechanical properties of Al-Cu-Mg-Ag sheets. *Mater. Lett.* **2012**, *66*, 311–313. [CrossRef]
26. Kocich, R.; Kursa, M.; Macháčková, A. FEA of Plastic Flow in AZ63 Alloy during ECAP Process. *Acta Phys. Pol. A* **2012**, *122*, 581–587. [CrossRef]

27. Cabibbo, M.; Paoletti, C.; Minárik, P.; Král, R.; Zemková, M. Secondary phase precipitation and thermally stable microstructure refinement induced by ECAP on Mg-Y-Nd (WN43) alloy. *Mater. Lett.* **2019**, *237*, 5–8. [CrossRef]
28. Kocich, R.; Kunčická, L.; Král, P.; Lowe, T.C. Texture, deformation twinning and hardening in a newly developed Mg–Dy–Al–Zn–Zr alloy processed with high pressure torsion. *Mater. Des.* **2016**, *90*, 1092–1099. [CrossRef]
29. Hlaváč, L.M.; Kocich, R.; Gembalová, L.; Jonšta, P.; Hlaváčová, I.M. AWJ cutting of copper processed by ECAP. *Int. J. Adv. Manuf. Technol.* **2016**, *86*, 885–894. [CrossRef]
30. Kunčická, L.; Kocich, R.; Dvořák, K.; Macháčková, A. Rotary swaged laminated Cu-Al composites: Effect of structure on residual stress and mechanical and electric properties. *Mater. Sci. Eng. A* **2019**, *742*, 743–750. [CrossRef]
31. Asadi, P.; Mahdavinejad, R.A.; Tutunchilar, S. Simulation and experimental investigation of FSP of AZ91 magnesium alloy. *Mater. Sci. Eng. A* **2011**, *528*, 6469–6477. [CrossRef]
32. Jamili, A.M.; Zarei-Hanzaki, A.; Abedi, H.R.; Minárik, P.; Soltani, R. The microstructure, texture, and room temperature mechanical properties of friction stir processed Mg-Y-Nd alloy. *Mater. Sci. Eng. A* **2017**, *690*, 244–253. [CrossRef]
33. Gan, W.M.; Huang, Y.D.; Wang, R.; Zhong, Z.Y.; Kainer, K.U.; Schell, N.; Brokmeier, H.-G.; Schreyer, B.A. Bulk and local textures of pure magnesium processed by rotary swaging. *J. Magnes. Alloy.* **2013**, *1*, 341–345. [CrossRef]
34. Gan, W.M.; Huang, Y.D.; Wang, R.; Wang, G.F.; Brokmeier, H.-G.; Schell, N.; Kainer, K.U.; Hort, N. Microstructures and mechanical properties of pure Mg processed by rotary swaging. *Mater.Des.* **2014**, *63*, 83–88. [CrossRef]
35. Wang, C.; Yu, Z.; Cui, Y.; Yu, S.; Ma, X.; Liu, H. Effect of hot rotary swaging and subsequent annealing on microstructure and mechanical properties of magnesium alloy WE43. *Met. Sci. Heat Treat.* **2019**, *60*, 777–782. [CrossRef]
36. Shabadi, R.M.; Ionescu, M.; Jeandin, M.; Richard, C.; Chandra, T. Strengthening of magnesium alloy WE43 by rotary swaging. *Mater. Sci. Forum* **2018**, *941*, 808–813. [CrossRef]
37. Martynenko, N.S.; Luk'yanova, E.A.; Morozov, M.M.; Yusupov, V.S.; Dobatkin, S.V.; Estrin, Y. A study of the structure, mechanical properties and corrosion resistance of magnesium alloy WE43 after rotary swaging. *Met. Sci. Heat Treat.* **2018**, *60*, 253–258, ISSN 1573-8973. [CrossRef]
38. Wang, Y.; Huang, Y.; Meng, X.; Wan, L.; Feng, J. Microstructural evolution and mechanical properties of MgZnYZr alloy during friction stir processing. *J. Alloys Compd.* **2017**, *696*, 875–883. [CrossRef]
39. Kumar, N.; Mishra, R.S.; Dahotre, N.B.; Brennan, R.E.; Doherty, K.J.; Cho, K.C. Effect of friction stir processing on microstructure and mechanical properties of laser-processed Mg-4Y-3Nd alloy. *Mater. Des.* **2016**, *110*, 663–675. [CrossRef]
40. Vargas, M.; Lathabai, S.; Uggowitzer, P.J.; Qi, Y.; Orlov, D.; Estrin, Y. Microstructure, crystallographic texture and mechanical behaviour of friction stir processed Mg–Zn-Ca-Zr alloy ZKX50. *Mater. Sci. Eng. A.* **2017**, *685*, 253–264. [CrossRef]
41. Liu, G.; Ma, Z.; Wei, G.; Xu, T.; Zhang, X.; Yang, Y.; Xie, W.; Peng, X. Microstructure, tensile properties and corrosion behavior of friction stir processed Mg-9Li-1Zn alloy. *J. Mater. Process. Technol.* **2019**, *267*, 393–402. [CrossRef]
42. Khan MD, F.; Karthik, G.M.; Panigrahi, S.K.; Janaki Ram, G.D. Friction stir processing of QE22 magnesium alloy to achieve ultrafine-grained microstructure with enhanced room temperature ductility and texture weakening. *Mater. Charact.* **2019**, *147*, 365–378. [CrossRef]
43. Oxford Instruments. Providing Leading-Edge Tools for SEM, TEM &FIB—Nanoanalysis. 2018. Available online: https://nano.oxinst.com/ (accessed on 24 December 2018).
44. Humphreys, F.J.; Hetherly, M. *Recrystallization and Related Annealing Phenomena*, 2nd ed.; Elsevier Ltd.: Oxford, UK, 2004.
45. Kocich, R.; Kunčická, L.; Dohnalík, D.; Macháčková, A.; Šofer, M. Cold rotary swaging of a tungsten heavy alloy: Numerical and experimental investigations. *Int. J. Refract. Met. Hard Mater.* **2016**, *61*, 264–272. [CrossRef]
46. Kunčická, L.; Kocich, R. Deformation behaviour of Cu-Al clad composites produced by rotary swaging. *IOP Conf. Ser. Mater. Sci. Eng.* **2018**, *369*, 012029. [CrossRef]

47. Li, J.; Zhang, D.-T.; Chai, F.; Zhang, W. Microstructures and mechanical properties of WE43 magnesium alloy prepared by friction stir processing. *Rare Met.* **2014**, 1–6. [CrossRef]
48. Verlinden, B.; Driver, J.; Samajdar, I.; Doherty, R.H. *Thermo-Mechanical Processing of Metallic Materials*; Elsevier: Amsterdam, The Netherlands, 2007.
49. Chang, C.I.; Lee, C.J.; Huang, J.C. Relationship between grain size and Zener–Holloman parameter during friction stir processing in AZ31 Mg alloys. *Scr. Mater.* **2004**, *51*, 509–514. [CrossRef]
50. Yuan, W.; Mishra, R.S. Grain size and texture effects on deformation behavior of AZ31 magnesium alloy. *Mater. Sci. Eng. A* **2012**, *558*, 716–724. [CrossRef]
51. Liu, Y.T.; Zhou, J.X.; Liu, Y.T.; Tang, S.Q. Effect of Rare-Earth Element Y on the Microstructure and Mechanical Properties of the Mg-6.0wt.%Zn-0.5wt.%Zr Alloy. *Mater. Sci. Forum* **2017**, *898*, 91–96. [CrossRef]
52. Pourbahari, B.; Mirzadeh, H.; Emamy, M. The Effects of Grain Refinement and Rare Earth Intermetallics on Mechanical Properties of As-Cast and Wrought Magnesium Alloys. *J. Mater. Eng. Perform.* **2018**, *27*, 1327–1333. [CrossRef]
53. Torroni, A.; Xiang, C.; Witek, L.; Rodriguez, E.D.; Coelho, P.G.; Gupta, N. Biocompatibility and degradation properties of WE43 Mg alloys with and without heat treatment: In vivo evaluation and comparison in a cranial bone sheep model. *J. Cranio Maxillofac. Surg.* **2017**, *45*, 2075–2083. [CrossRef]

© 2019 by the authors. Licensee MDPI, Basel, Switzerland. This article is an open access article distributed under the terms and conditions of the Creative Commons Attribution (CC BY) license (http://creativecommons.org/licenses/by/4.0/).